Biophysical Journal Volume 74 January 1998 645–654

# Birefringence of Single and Bundled Microtubules

R. Oldenbourg,* E. D. Salmon,*# and P. T. Tran*#

*Marine Biological Laboratory, Woods Hole, Massachusetts 02543, and #Department of Biology, University of North Carolina, Chapel Hill, North Carolina 27599-3280 USA

ABSTRACT We have measured the birefringence of microtubules (MTs) and of MT-based macromolecular assemblies in vitro and in living cells by using the new Pol-Scope. A single microtubule in aqueous suspension and imaged with a numerical aperture of 1.4 had a peak retardance of 0.07 nm. The peak retardance of a small bundle increased linearly with the number of MTs in the bundle. Axonemes (prepared from sea urchin sperm) had a peak retardance 20 times higher than that of single MTs, in accordance with the nine doublets and two singlets arrangement of parallel MTs in the axoneme. Measured filament retardance decreased when the filament was defocused or the numerical aperture of the imaging system was decreased. However, the retardance "area," which we defined as the image retardance integrated along a line perpendicular to the filament axis, proved to be independent of focus and of numerical aperture. These results are in good agreement with a theory that we developed for measuring retardances with imaging optics. Our theoretical concept is based on Wiener's theory of mixed dielectrics, which is well established for nonimaging applications. We extend its use to imaging systems by considering the coherence region defined by the optical set-up. Light scattered from within that region interferes coherently in the image point. The presence of a filament in the coherence region leads to a polarization dependent scattering cross section and to a finite retardance measured in the image point. Similar to resolution measurements, the linear dimension of the coherence region for retardance measurements is on the order $\lambda/(2\ \mathrm{NA})$, where $\lambda$ is the wavelength of light and NA is the numerical aperture of the illumination and imaging lenses.

## INTRODUCTION

The living cell is criss-crossed by dense networks of filaments providing mechanical stability, site-directed molecular and organellar transport, and support of other vital cell functions. Filaments such as microtubules reorganize in the living cell into different networks depending on the state of the cell. For example, during cell division microtubules organize into a dense array of aligned filaments and thick bundles forming the mitotic spindle (Fig. 1), whereas at other times, microtubules span the cytoplasm as a network of individual filaments. Because of the pervasive nature of filaments in the living cell, their reorganization into different kinds of networks, and their vital role in cell functions, the visualization of this dynamic network architecture is very important for understanding the molecular biology of the cell.

With polarized light microscopy we can observe the birefringence associated with thin filaments or partially oriented filament networks and measure the birefringence directly in the living cell. Filament birefringence is a consequence of their elongated shape, whether or not their subunit molecules are anisotropic, and occurs naturally without the need to stain or label them, as is necessary in fluorescence imaging. With the new Pol-Scope, which we have developed (Oldenbourg and Mei, 1995; Oldenbourg, 1996), birefringence is measured at high sensitivity and high resolution, quantifying image information to the level of individual microtubules (Tran et al., 1995).

Polarized light microscopy was long recognized as a powerful analytical tool for measuring submicroscopic molecular order in biological as well as other specimens (Chamot and Mason, 1958; Hartshorne and Stuart, 1960; Inoué, 1986, Appendix III; McCrone, 1991). Inspired by W. J. Schmidt, who made many pioneering observations on the structure and development of skeletal and cellular components using polarized light (Schmidt, 1924, 1937), Shinya Inoué, in 1953 at the Marine Biological Laboratory in Woods Hole, was the first to demonstrate the filamentous nature of the mitotic spindle directly in living cells by using time-lapse movies recorded with the polarizing microscope (Inoué, 1953). Later, he and his colleagues demonstrated that microtubules are the sole contributor to spindle birefringence and established a relationship between spindle retardance and microtubule density (Sato et al., 1975). The introduction of video-enhanced microscopy by Inoué (1981) and by Allen et al. (1981) made it possible to visualize individual microtubules reconstituted in solution (Allen and Allen, 1983) or decorated with gold particles in the dividing cell (Inoué et al., 1985; Inoué and Spring, 1997, Color Plate III). A quantitative study of microtubule birefringence using a flow apparatus was published by Hard and Allen (1985).

Most of the earlier measurements of microtubule birefringence considered arrays of parallel or partially aligned MTs. The interpretations of these measurements were based on optical concepts that are not readily transferable to imaging systems. When individual filaments were visualized, no attempt was made to interpret microtubule birefringence quantitatively. With the advent of the Pol-Scope, a quantitative birefringence imaging system, we have a tool that can

---

*Received for publication 28 April 1997 and in final form 30 July 1997.*

Address reprint requests to Dr. Rudolf Oldenbourg, Marine Biological Laboratory, Woods Hole, MA 02543-1015. Tel.: 508-289-7426; Fax: 508-540-6902; rudolfo@mbl.edu.

0006-3495/98/01/645/10 $2.00

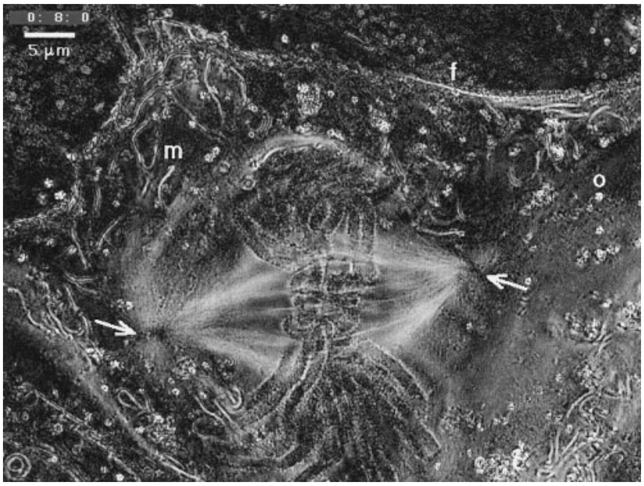

FIGURE 1 Newt lung epithelial cell in mitosis (retardance magnitude image). Bright spindle fibers made up of microtubules locate the large chromosomes between the spindle poles (*arrows*). Chromosomes are outlined by birefringence near their edges. Elongated mitochondria (m), long stress fibers (f), and small, spherical organelles (o) can also be seen surrounding the spindle.

consistently measure retardances down to 0.02 nm, independent of slow axis orientation, and visualize single microtubules well above the noise level. This article describes birefringence measurements on single microtubules and bundles of microtubules and develops a quantitative theory for the interpretation of these measurements. In the Materials and Methods section we include the description of some instrumental factors that are critical to the success of measuring the exceedingly small retardance of single microtubules and of other fine macromolecular structures. We then present the microtubule measurements, including the dependence of the measured retardance on image focus. In contrast to the peak retardance, which decreased quickly when the object defocused, we found a new quantity, the retardance area, which was independent of focus and, somewhat surprisingly, of the NA of the objective lens. The Theory section provides a quantitative interpretation of these results, including the new parameter of retardance area.

## MATERIALS AND METHODS

### Polarized light microscopy

Birefringence measurements were made with a new polarized light microscope (Pol-Scope; Oldenbourg and Mei, 1995; Oldenbourg, 1996). Briefly, the design of the Pol-Scope is based on the traditional polarized light microscope. The crystal compensator is replaced by a universal compensator made from two liquid crystal retarders (Cambridge Research and Instrumentation, Cambridge, MA) oriented with their slow axes at 45° to each other. The liquid crystals are placed in the illumination path following the linear polarizer. The retardance of the two liquid crystals can be controlled electrically and is typically set to a quarter-wave and half-wave, respectively, to produce right circularly polarized light. The polarized light is focused into the sample by the condenser, and the objective lens projects an image of the sample onto a CCD video camera. A left circular analyzer is placed between the objective and the CCD camera and blocks most of the background light. To measure specimen birefringences, the liquid crystal retardances are detuned slightly to produce a sequence of three elliptical polarizations of small and equal ellipticity and differing orientations of their principal polarization axes. The three images, recorded with elliptical polarization together with one in circularly polarized light (compensator not detuned), are then used to calculate the specimen retardances in each image point simultaneously, as described by Oldenbourg and Mei (1995).

High NA lenses, as used in this study, typically introduce polarization aberrations that can severely reduce sensitivity and fidelity of image detail in polarized light microscopy (Inoué and Hyde, 1957; Kubota and Inoué, 1959). However, the effect of polarization aberrations seems to be diminished in the new Pol-Scope, which uses nearly circularly polarized light and applies a background correction procedure. Nevertheless, when using immersion lenses with NAs higher than 1.0, we set the condenser aperture to no more than 1.0 NA, blocking the high NA illumination rays, which carry the most severe polarization aberrations and significantly reduce the extinction and sensitivity of the set-up. A 1.0 condenser NA was a practical compromise between maintaining the resolution and sensitivity that decreased when the condenser aperture was opened further. The optimal setting does depend on the actual lenses used, which can carry different amounts of stress and birefringent inclusions in their lens elements, and antireflection coatings on lens surfaces, which can also affect the amount of polarization aberrations introduced by a compound lens. For best results it is advisable to use condenser and objective lenses that were carefully selected for low polarization aberrations. Furthermore, oil or water immersion lenses are preferred because they eliminate or reduce the refractive index mismatch and spherical aberration that can be introduced by the air space between coverslip or glass slide and front elements of dry objective or condenser lenses.

The following is a list of some additional optical parts and settings used for the current study. We used an apochromat, oil immersion condenser lens with aperture diaphragm (max. NA 1.4) and, typically, a 60×/1.4 NA Plan Apochromat objective lens, both selected for low polarization aberrations (Nikon, Melville, NY); a mercury arc lamp followed by an Ellis light scrambler (Technical Video, Woods Hole, MA) to homogeneously illuminate the back aperture of the condenser (Inoué, 1986); a narrow band pass interference filter (546 nm, 10 nm FWHM; Omega, Brattleboro VT) to select the green mercury line for intense monochromatic illumination; and a liquid crystal detuning parameter (swing value) of 16 nm to measure filament birefringences.

Focus levels were adjusted by driving the microscope stage with a stepper motor (Microphot SA with remote focus accessory; Nikon) under computer control and a minimum step size of 0.1 $\mu$m in the axial direction. The accuracy and repeatability of focus settings were checked by using nanofabricated test targets (Oldenbourg et al., 1996) and coverslips of known thickness. To avoid backlash, we always approached a given focus or $z$ position from the same direction, lifting the stage from a lower position to the desired $z$ position. Distances along the optical axis of the microscope ($z$ axis) are given as distances traveled by the microscope stage.

For instrument control, image acquisition, processing, and display, we used a Macintosh desktop computer (Power PC 8500; Apple Computer, Cupertino, CA) with averaging frame grabber board (AG-5; Scion Corp., Frederick, MD) and public domain image-processing software (NIH Image, developed at the U.S. National Institutes of Health and available on the Internet at http://rsb.info.nih.gov/NIH-image), which was enhanced by custom-written software functions. Video images captured with a scientific grade CCD camera (C72; Dage-MTI, Michigan City, IN) were digitized to 8 bits, 640 pixels wide and 480 pixels high. To record images with the least amount of intensity noise, the camera gain was set to its minimum to reduce amplifier noise. Light levels were generally sufficient, so that recorded images used the full video signal range, even with the camera gain set to a minimum. If light levels were insufficient, on-chip integration was used to boost the video signal. In all cases, eight consecutive frames were averaged to minimize camera read noise. Special software was written by Scion Corp. to provide control signals on the frame grabber AG-5 for on-chip integration, frame averaging, and liquid crystal detuning. These functions were synchronized to the video signal and achieved data collection without unnecessary loss of video frames. The frame acquisition procedure resulted in images with nearly eight significant bits for each pixel. Image magnification could be adjusted by a zoom lens (zoom ratio 2.25/0.9; Nikon) placed between the analyzer and the CCD camera. Most images used in this study were recorded with a zoom factor of 2.25 and a 60× objective magnification, which resulted in a measured object space resolution of 77 nm per pixel. The optical resolution, using the same lenses, was about three pixels wide or 230 nm (≈ 546 nm/(1.4 + 1.0); Inoué and Oldenbourg, 1995).

The fastest acquisition time for a single set of four raw images was at least 13 frame times or 0.43 s. This time is primarily determined by the speed of the liquid crystals as they settle to a new retardance level, which takes ~0.1 s or three frame times. The time span proved to be too long to image single microtubules that are free to move as Brownian particles. In a set of four images, freely moving MTs produce misregistrations, which lead to erroneous retardance calculations. In the future, we expect improvements in liquid crystal design and/or the use of Pockel cells to alleviate this problem. In living cells, however, Brownian motion is generally sufficiently reduced by the viscoelastic properties of the cytoplasm that misregistrations at current liquid crystal speeds are not a problem.

The displayed Pol-Scope images represent optical anisotropies in the sample measured as retardance magnitude in each picture element and are visualized as gray values. Black areas in the image represent zero retardance, and bright image features have finite retardance, independent of slow axis orientation of the sampled spot. The maximum retardance, mapped into white, is set individually for each image. In a given image, retardance values lower than the maximum are mapped linearly into the appropriate gray values, and higher retardance values are shown as white. In addition to the magnitude of retardance, the Pol-Scope also measures the orientation of the slow axis or azimuth angle of retardance measured for each pixel. The azimuth can be shown either in a separate image, or merged with the magnitude information, using color or lines to visualize the orientation. When printed, the azimuth angle is given in degrees and is measured from the horizontal axis (positive $x$ axis). The frame acquisition procedure described earlier recorded images with a minimum of intensity noise. The remaining intensity noise resulted in a retardance noise floor with an average magnitude of 0.02 nm and random slow axis orientation for regions showing less than 0.02 nm retardance. The variations in measured microtubule and axoneme retardances were typically higher, possibly because of differences in preparation and exact focus level.

## Tubulin and axoneme preparation

Tubulin was purified by the methods of Voter and Erickson (1984) and Walker et al. (1988). Briefly, porcine brain was homogenized and centrifuged through three cycles of warm-cold assembly-disassembly in PEM buffer (100 mM PIPES, 2 mM EGTA, 1 mM $MgSO_4$, pH 6.9) + 0.5 mM GTP. The resulting pellets were resuspended in PEM buffer and passed over an ion exchange phosphocellulose column. The tubulin eluate was further purified by assembly at 37°C with 1 M Na-glutamic acid, and then resuspended in PEM buffer containing 0.5 mM GTP and stored at −80°C. This was the stock GTP-tubulin used in all experiments.

Axonemes were purified by the method of Bell et al. (1982). Briefly, *Lytechinus pictus* sperm flagellar axonemes were osmotically demembranated in a 20% sucrose solution and separated from sperm heads with a homogenizer. Axoneme pellets were then washed in a low salt buffer (100 mM NaCl, 4 mM $MgSO_4$, 1 mM EDTA, 10 mM HEPES, 7 mM $\beta$-mercaptoethanol, pH 7.0), and dynein arms were removed by suspending pellets in a high salt buffer (600 mM NaCl, 4 mM $MgSO_4$, 1 mM EDTA, 10 mM HEPES, 7 mM $\beta$-mercaptoethanol, pH 7.0). Axonemes were further purified by sedimentation through an 80% sucrose solution. Purified axonemes were stored in 1:1 low salt:glycerol solution at −20°C. Before being used, axonemes were washed twice and resuspended in PEM buffer. All chemical reagents mentioned were supplied by Sigma (St. Louis, MO).

## Imaging assay

Purified tubulin (≈ 50 μM) was allowed to spontaneously self-assemble into microtubules by incubating in a 37°C water bath for 15 min. The self-assembled microtubules were then stabilized and diluted by adding PEM buffer containing 10 μM taxol. Vigorous shaking of the preparation produced stabilized microtubule fragments with 10–20-μm lengths, ideal for subsequent imaging.

A chamber was produced by introducing two strips of Double-Sticky tape (3M, St. Paul, MN) as spacers between a clean glass slide (Clay Adams, Lincoln Park, NJ) and a biologically clean 22 × 22 mm coverslip (Corning, Corning, NY), 0.17 mm thick. This chamber was necessary for the perfusion of the microtubules or axonemes, and subsequent wash-through with PEM buffer to ensure a clean preparation devoid of contaminating particulates that might interfere with the imaging.

While the axoneme samples readily adhered to the coverslip surface of the chamber, the microtubules did not, and instead exhibited Brownian motion, making imaging difficult. To make the microtubules adhere to the coverslip surface, the kinesin-like motor protein Kar3 was perfused through the chamber first. They stick to the coverslip surface, and subsequently bind to and immobilize the microtubule on the coverslip surface. The Kar3 proteins used in this study had only microtubule binding activity and lacked microtubule translocation activity (Endow et al., 1994).

# MEASURED RETARDANCES OF SINGLE AND BUNDLED MICROTUBULES

## Peak retardance

With the Pol-Scope we have imaged single microtubules (MTs) and small bundles of MTs (Fig. 2) (Tran et al., 1995)), which adhered to the coverglass surface (see Materials and Methods). Using the 60×/1.4 NA Plan Apo objective, we measured a peak retardance of 0.07 ± 0.02 nm (30 measurements) for single MTs, with the slow axis oriented parallel to the filament axis. For bundles of two or three MTs, the peak retardance increased linearly with the number of MTs (Fig. 2).

For single axonemes prepared from sea urchin sperm (see Materials and Methods), we measured a peak retardance of 1.43 ± 0.1 nm (Fig. 3), using the same objective lens. Hence an axoneme has a peak retardance that is 20.4 times higher than the one we found for a single microtubule. The number 20.4 compares well with the 9 + 2 arrangement of microtubules in axonemes, which contain nine doublets and two individual MTs. A doublet is made up of one complete microtubule and one partial microtubule, which in traverse section shows 11 of 13 subunits (Dustin, 1984). Therefore we estimate the equivalent number of complete microtubules in an axoneme to be $9 * (1 + 11/13) + 2 = 18.6$. The difference from 20.4 is probably due to proteins such as tektin, which forms a microtubule-associated filament in sperm axonemes (Linck et al., 1985).

The retardance magnitude image of an axoneme (Fig. 3 *A*) is composed of a central bright line flanked on either side by weaker lines. The weaker lines have about one-third of the retardance magnitude of the central line and are due to diffraction. These subsidiary maxima constitute an imaging artifact, which must not be confused with real structure in the specimen (Oldenbourg, 1991). The central line contains the peak retardance, which has its slow axis parallel to the

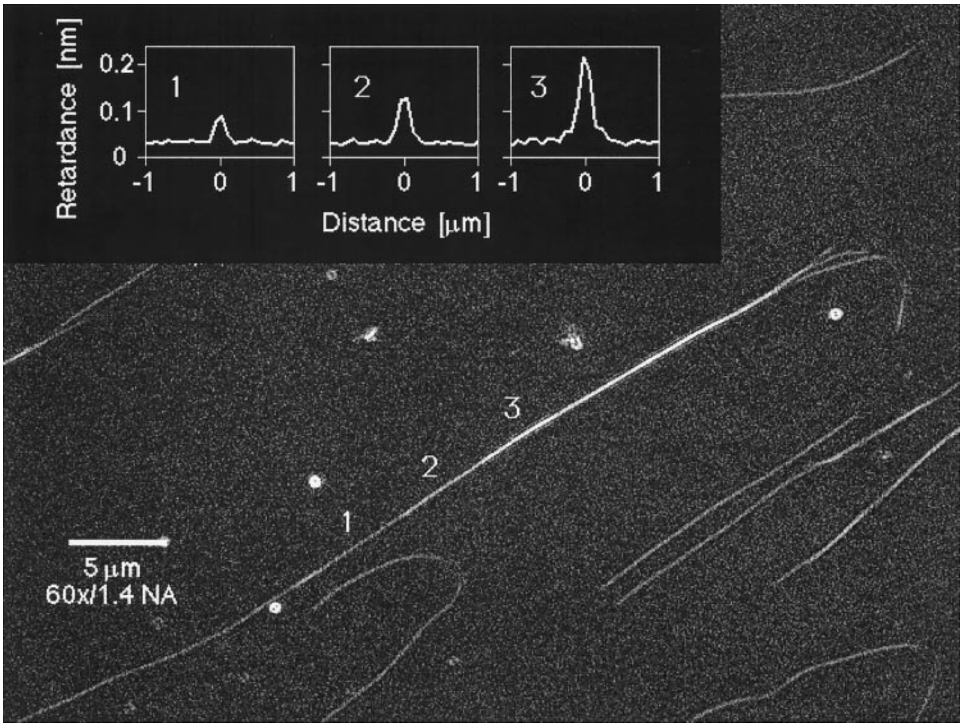

FIGURE 2 Spontaneously assembled microtubules, stabilized with taxol, adhered to the coverglass surface and were imaged with the new Pol-Scope (retardance magnitude). Most filaments are single microtubules (MT), with the exception of one bundle containing one, two, and three MTs. The inset shows line scans across the filament axis at locations with one, two, and three MTs. Note that at the top right end, the bundle sprays into three individual microtubules. (In the figure, MT birefringence is sometimes reduced near turns of the MT filament. This reduction is probably caused by the microtubule lifting off the coverglass. MT parts that are lifted off the coverglass are out of focus and therefore have a reduced peak retardance).

filament axis (Fig. 3 *B*). We say that the central retardance is positive. The flanking weaker lines, however, have their slow axes oriented perpendicular to the filament axis, and their retardance is negative. We carefully established that slow axis orientations in the central and subsidiary maxima of a filament image are either parallel or perpendicular to the filament axis, in contrast to background retardances, which have a random distribution of azimuth angles (Fig. 3 *B*). Based on this finding, we plotted image retardances measured at different distances from the filament center in terms of positive and negative retardances (Fig. 4, projected retardance graphs). The retardance in every position was calculated by projecting the measured retardance onto the orientation parallel to the filament axis, using the formula $R_{\mathrm{proj}} = |R| \cos(2\Delta)$, where $|R|$ is the retardance magnitude and $\Delta$ is the angle between the filament axis and the slow axis direction. $\cos(2\Delta)$ is positive for $\Delta$ near zero and is negative for $\Delta$ near 90°. Hence this projection algorithm renders retardances positive if their slow axes are more parallel to the filament axis, whereas they become negative if their slow axes are more perpendicular to the filament axis. Because background retardances have random azimuth values, their projections vary between positive and negative numbers and average out to zero. All line scans obtained in this study, including the projected retardances, were averaged along the length of the filament over a distance of 1.5 μm (20 pixels).

### Focus series and retardance area

The peak retardance measured in a single filament depended on the focus position adjusted with the microscope stage (Fig. 4). Lowering or raising the stage by 0.2 μm away from the best focus position reduced the measured peak retardance by almost a factor of 2 (60×/1.4 NA Plan Apo objective). Moving the stage in either direction by 0.6 μm reduced the peak retardance by a factor of 10.

During defocusing, the peak retardance is reduced, and as expected, the width of the filament image increases. This observation is similar to image records showing, for example, the fluorescence intensity in a labeled filament. The aberration-free image of the labeled filament is sharpest, i.e., the peak intensity is highest and the width smallest, when the filament is in focus. Defocusing reduces the peak height and broadens the width in such a way that the total fluorescence intensity recorded over a given filament length is independent of the focus position (Wilson and Sheppard, 1984). This holds true within certain limits for wide field, nonconfocal imaging, and is simply an expression of the conservation of fluorescence intensity collected by the objective lens. In analogy to this observation in fluorescence microscopy, we attempted to determine whether a similar statement can be made for the measured retardance of a filament. To this end we analyzed line plots, such as the ones in Fig. 4, for the area under the retardance curve. The retardances to the left and right of the filament image were considered background, and their linear interpolation defined zero retardance at different distances (the subsidiary maxima were considered a negative part of the filament image). Then filament values were added up, with retardances below the background counting as negative (subtracting) and those above the background counting as positive (adding) toward the sum. The resultant retardance area has the dimension $\mathrm{nm}^2$, one nm for the dimension of retar-

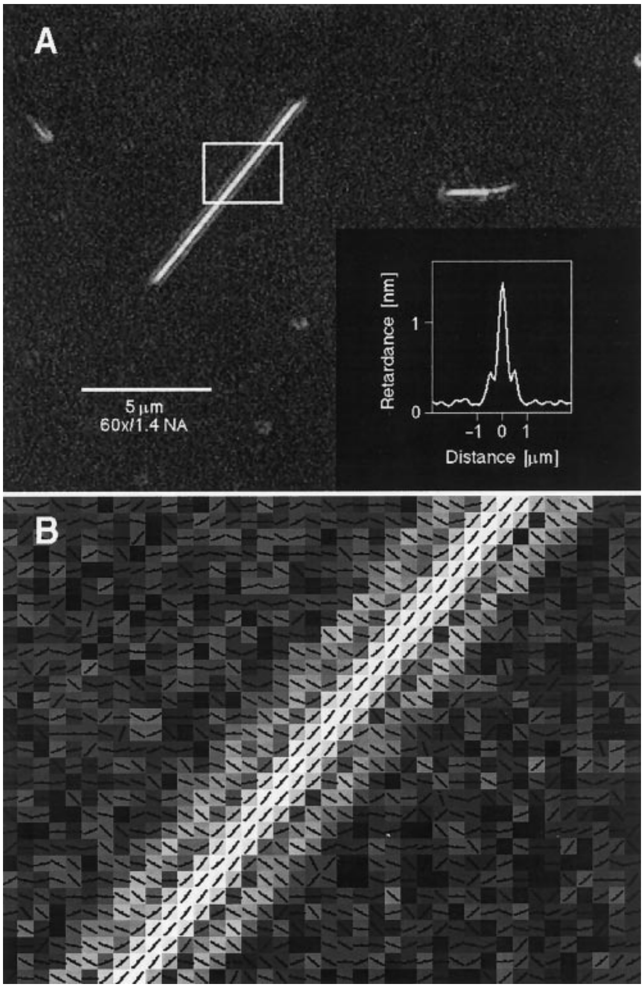

FIGURE 3 Purified, dynein-free axonemes of sea urchin sperm. (*A*) Retardance magnitude image shows central bright line flanked by two subsidiary maxima, which are caused by diffraction. The inset shows a line scan across the filament axis. (*B*) Magnified portion of *A*, with added lines indicating the measured slow axis orientation in each pixel. The central axoneme retardance has parallel slow axis orientation, whereas the subsidiary maxima have perpendicular slow axis orientation.

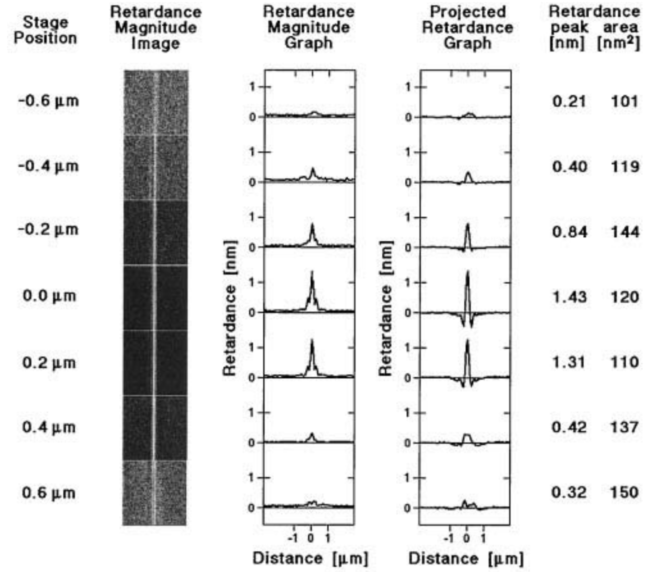

FIGURE 4 Retardance images and graphs of an axoneme recorded at different focus positions (*z* positions; *z* is set to zero for the focus position that recorded the highest peak retardance). The column of retardance magnitude images shows the variation in image detail dependent on focus (images are contrast enhanced for better visibility). The retardance magnitude graphs are line scans across the filament axes. The graphs of projected retardances show central retardances as positive (slow axes parallel to the filament), whereas subsidiary maxima have negative birefringence (slow axes perpendicular to the filament). The graphical data show the decrease in peak retardance and the broadening of the image with increasing defocus. The numbers on the right give the measured peak retardances and areas under the projected retardance curves.

dance and the other for the dimension of distance over which the retardance was summed up (integrated). In practical terms, the retardance area is the sum of the projected retardances measured in pixels along a line perpendicular to the filament axis minus the interpolated background values and times the scale factor nm/pixel mentioned in Materials and Methods. In Fig. 4 we show values of the retardance area measured in a single focus series, and in Fig. 5 we present the results of many measurements which demonstrate that the retardance area is indeed independent of the focus position.

The results shown in Fig. 5 were obtained by using a single objective lens (40× Fluor oil immersion; Nikon) that incorporates an adjustable diaphragm to change the effective objective NA between 0.5 and 1.3. The condenser NA was set equal to the objective NA, except for NAs larger than 1.0, when the condenser NA was kept constant at 1.0 to reduce polarization aberrations (see Materials and Methods). The measurements shown in Fig. 5 clearly demonstrate that the retardance area is not only independent of the focus position, but also of the numerical aperture used to image the filaments. For axonemes we measured an average retardance area of 150 nm$^2$. We find the retardance area for single microtubules by dividing 150 by 20 to arrive at 7.5 nm$^2$, noting that the retardance area scales the same way as the peak retardance.

## Crossing axonemes

We have shown that the retardance of bundles of microtubules increases linearly with the number of MTs in the bundle. Hence, for parallel arrangement of filaments, the individual filament retardances add to the bundle retardance. If, however, two filaments are perpendicular to each other, we expect their retardances to subtract, similar to two birefringent crystal plates that are in subtractive positions. Fig. 6 shows images of two axonemes that cross each other. The results presented in the figure support this expectation. The measured retardance in the central overlap region is indeed reduced, but is not zero. This is due in part to the inexact perpendicular arrangement of the axonemes. More importantly, the two axonemes are displaced in the *z* direction, and therefore the peak retardances occur at different

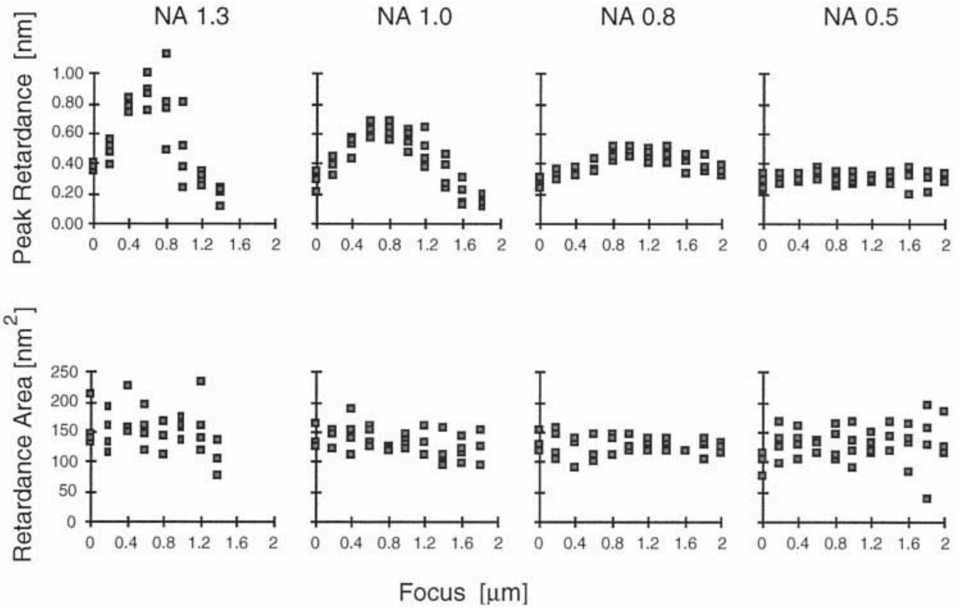

FIGURE 5 Peak retardances and area under projected retardance curves measured for several axonemes, using an objective lens with a built-in aperture diaphragm to adjust for different NAs. Graphs in the top row show peak retardances measured at different focus levels and with different objective NAs. (Focus levels are given with respect to an arbitrary reference point.) The peak retardance clearly decreases with decreasing NA and with increasing distance from the ideal focus. The bottom row shows retardance areas at different focus levels and NAs, demonstrating that, within measurement uncertainties, the area is independent of focus and NA.

focus levels. This interpretation is also supported by the measured slow axis orientation in the central overlap region, which flips from being parallel to one axoneme to being parallel to the other axoneme, depending on the focus level (Fig. 6). Somewhat surprising is the relatively large $z$ displacement of ~0.4 μm (400 nm) between the focus levels of the first and second axonemes in the crossing point. If our interpretation depicted in the top right schematic of Fig. 6 is correct, the two axonemes touch each other at the crossing point, and their center lines are displaced along $z$ by no more than the axoneme diameter. The diameter of dehydrated axonemes prepared for electron microscopy is ~175 nm (Tilney et al., 1973). Biological assemblies tend to shrink during dehydration; therefore the hydrated axonemes of our experiments might have a slightly larger diameter. In addition, the seemingly large distance in $z$ is partly caused by the refractive index mismatch at the interface between the coverglass and the aqueous medium. It is well known that the focus of a converging light cone that traverses a glass-water interface and comes to a focus on the low refractive index (water) side of the interface is shortened. The distance between focus and interface is shortened by the refraction of light at the interface. There is a similar reduction in the change in distance between focus and interface when moving the interface either closer or farther away from the focus. As described by Visser et al. (1992), when the interface position is changed by raising the microscope stage over a length $\Delta z$, the distance between focus and interface changes by less than $\Delta z$. The exact amount of reduction depends on the cone angle of light rays considered. For paraxial rays the ratio of stage travel to focus change is the ratio of the refractive indices of glass to water ($1.52/1.33 = 1.14$), whereas for marginal rays of a 1.3 NA oil immersion lens the distance ratio increases to more than 2.5 (Visser et al., 1992). Because the image of microtubules with subwavelength diameter is primarily formed by high NA rays, it seems reasonable to measure an apparent $z$ distance that is larger by up to a factor 2 than the physical distance between the axonemes.

## THEORY OF SINGLE FILAMENT RETARDANCE

In this section we develop the theoretical concept that allows us to estimate the birefringence of single and bundled microtubules that we measured using a high numerical aperture imaging system. We base our estimate on the theory of mixed dielectrics, which was developed by Wiener (1912) and was extended recently by Oldenbourg and Ruiz (1989). The theory was developed for dielectric particles of anisotropic shape (e.g., rods) that are aligned parallel and suspended in a medium that, in general, has a refractive index different from that of the rodlets. Hence the theory strictly applies only to a suspension of large numbers of particles and to the computation of the birefringence of the suspension as a whole. However, by considering the appropriate sample volume probed by microscope optics, we can extend the applicability of the theory to single particle measurements and we can correctly predict the magnitude of microtubule birefringence and its dependence on the numerical aperture of the imaging system. The critical estimate in the theory is the volume of the coherence region that contributes to the measured retardance. We will first discuss this question for traditional birefringence measurements that use nonimaging optics and then give a quantitative estimate for measurements that employ finite-aperture lenses.

Birefringence is typically measured by using a relatively large sample volume, which is sandwiched between polarizing components (polarizer, compensator, analyzer) and

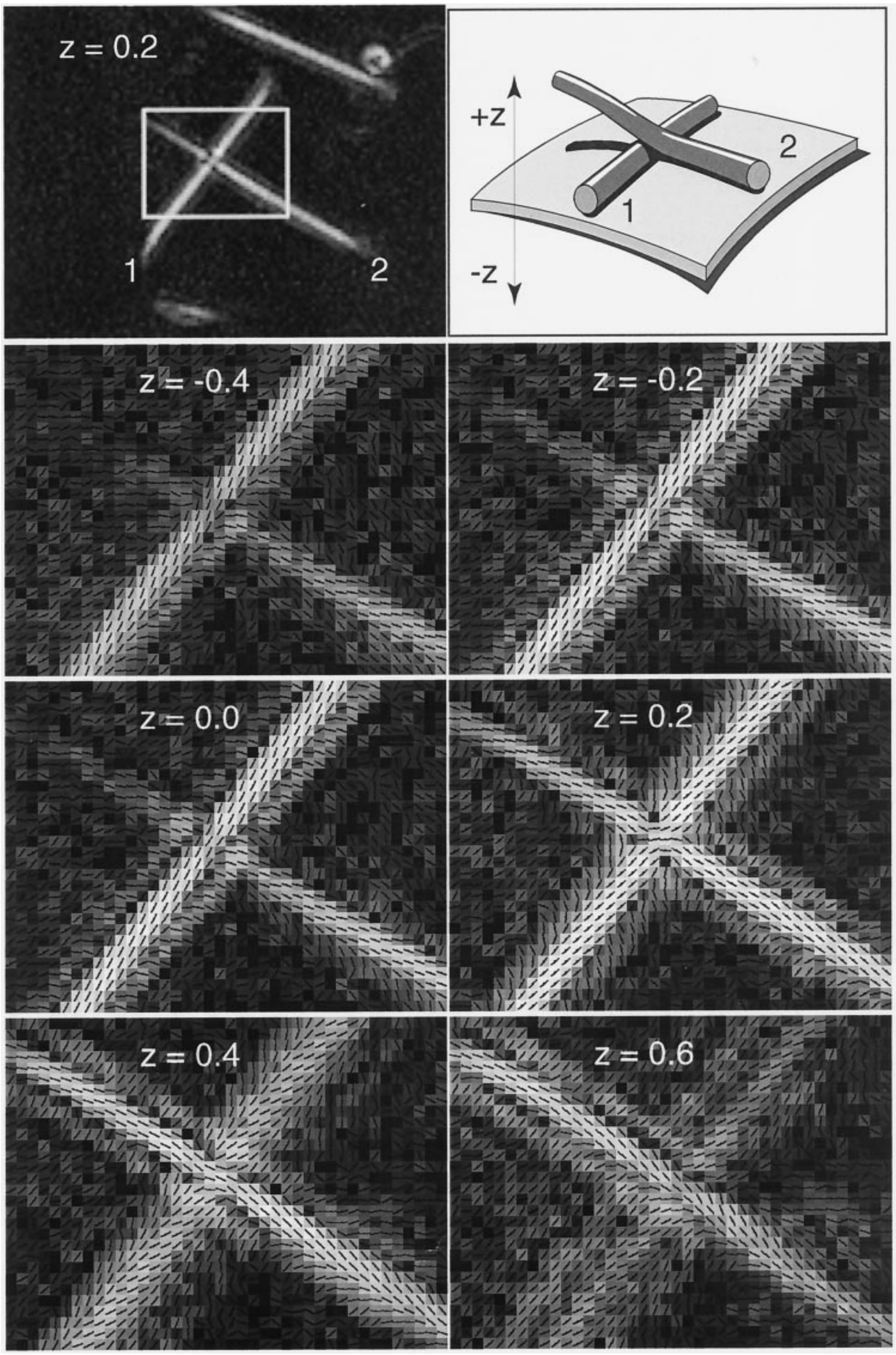

FIGURE 6 Top left image shows two axonemes that cross each other while adhering partly to the cover glass. The top right drawing depicts the arrangement of the two axonemes as derived from the focus series shown in the images below. The focus level of each image is given as a *z* value in $\mu$m ($z = 0$ for focus at cover glass surface, positive *z* for focus positioned in aqueous medium with axonemes, negative *z* for focus positioned inside cover glass). The images in the enlarged focus series show the magnitudes and slow axis directions, as in Fig. 3 *B*. Of particular interest are the pixels located in the crossing point of the two axonemes. Generally, where the centers of the axoneme images overlap, the magnitude is reduced because the two axonemes are in the subtractive position and their retardances compensate each other. Where a center overlaps with a subsidiary maximum, however, the measured retardance is increased, because the slow axes of these two image features are nearly parallel to each other. In addition to these observations on the magnitude one notices in the central area of the overlap a change in slow axis direction depending on focus position. For focus positions near or below the cover glass surface, the slow axis direction is parallel to axoneme 1, whereas for *z* positions at 0.4 $\mu$m and above, the slow axis is parallel to axoneme 2. From these observations we deduced the arrangement depicted in the schematic at the top right.

traversed by a nearly parallel beam of light. In general, the light beam changes its polarization state when it travels through the sample, which is characterized by its birefringence $\Delta n$ and thickness $d$. The birefringence $\Delta n$ is the difference of the refractive index for two orthogonally polarized light beams, $\Delta n = n_e - n_o$, where $n_o$ is the refractive index of the ordinary beam and $n_e$ is that of the extraordinary beam (we note that throughout this article we are concerned with linear birefringence). The product between birefringence and thickness, $\Delta n \cdot d$, is called retardance (Shurcliff, 1962), which directly measures the relative change in phase between the two orthogonally polarized light beams after they traversed the sample along its thickness $d$. Physically, the relative phase change comes about by the difference in speed of the two beams. Compared to their speed in a vacuum, the speed of both beams is reduced, but the polarization with the higher refractive index is slowed down more than the polarization with the lower refractive index. The reduction in the speed of light in dielectric media is a consequence of the interference between the light scattered by the medium and the unscattered beam. The forward or zero angle scattering interferes with the unscattered wave and retards the combined wave front, leading to a reduction in speed (Hecht, 1987). Hence a difference in scattering power of the medium for the two polarization directions leads to a difference in refractive index and to birefringence, $\Delta n$.

Interference phenomena can only occur between coherent or partially coherent light fields. For near-zero angle scattering, coherence is maintained over long distances because the scattered light field travels parallel to the exciting light beam and maintains a fixed phase relationship with the incoming field. Hence the extent of the optical coherence region in parallel beam measurements is very large and is practically defined by the dimensions of the sample. The scattering off all of the sample parts along the optical path interferes coherently at the detector and contributes to the measured retardance. Therefore, the amount of retardance is proportional to the thickness of the sample.

When a subwavelength particle is imaged, the situation is different. The extent of the coherence region is set by the numerical aperture NA of the illuminating and imaging lenses and by the wavelength of light $\lambda$ (Born and Wolf, 1980, Chapter 10; we assume that condenser and objective lenses have the same NA, as is the case in most of our experiments). We approximate the size of the coherence region with the shape of the central region of the diffraction image of a point object, which is also called the point spread function of the optical set-up. The shape of the central part is a cigarlike prolate. The prolate has a circular cross section with radius $\lambda/(2\mathrm{NA})$ in the plane perpendicular to the microscope axis, and extends over a distance of $(2n\lambda)/(\mathrm{NA}^2)$ parallel to the microscope axis (Inoué and Oldenbourg, 1995; $n$ is the refractive index of the sample medium). The scattered waves emanating from a sample region of this shape add coherently to form the conjugate image point. If the coherence region contains a thin filament, the scattering from this region will depend on polarization and will lead to a finite retardance measured in the image point.

To estimate the image retardance, we first estimate the volume fraction of the filament in the coherence region. The total volume of the coherence region is approximately its cross section times its length, $(\lambda/(2\mathrm{NA}))^2 \cdot (2n\lambda)/(\mathrm{NA}^2)$. Considering a long filament contained partially within the coherence region and oriented perpendicular to the microscope axis, we estimate the filament volume inside the region by multiplying its volume per unit length $\bar{V}$ times the linear dimension of the cross section, $\bar{V} \cdot \lambda/(2\mathrm{NA})$. Hence its volume fraction $f$ is

$$f = \frac{\bar{V} \cdot (\lambda/(2\mathrm{NA}))}{(\lambda/(2\mathrm{NA}))^2 \cdot (2n\lambda)/(\mathrm{NA}^2)} \tag{1}$$

We proceed by calculating the dielectric constant of the coherence region for light that is polarized parallel ($\epsilon_\parallel$) or perpendicular ($\epsilon_\perp$) to the filament axis. The calculation uses dielectric constants $\epsilon$ instead of refractive indices $n$, with the general relationship $\epsilon = n^2$, and is based on results first obtained by Wiener and later by others for the dielectric properties of suspensions of long thin rods in an isotropic solvent (Wiener, 1912; Bragg and Pippard, 1953; Oldenbourg and Ruiz, 1989):

$$\epsilon_\parallel = \epsilon_s + f(\epsilon_m - \epsilon_s), \tag{2}$$

$$\epsilon_\perp = \epsilon_s + \frac{f(\epsilon_m - \epsilon_s)}{1 + (1 - f)\dfrac{\epsilon_m - \epsilon_s}{2\epsilon_s}} \tag{3}$$

where $\epsilon_s$ and $\epsilon_m$ are the dielectric constants of the solvent and filament material, respectively. $f$ is the volume fraction of the filament in the coherence region. Physically, the difference between $\epsilon_\parallel$ and $\epsilon_\perp$ arises from the difference in the depolarizing fields when a filament is exposed to an electric field either parallel or pendicular to its axis. The depolarizing field is caused by the charges induced at the interface between the filament and the solvent. For parallel orientation, the depolarizing field is close to zero because the induced charges arising at opposite ends of the filament are far apart, whereas for perpendicular orientation of the field the charges induced on the filament surface are only a filament diameter apart and cause a depolarizing field that reduces the polarization of the filament. The denominator in Eq. 3 expresses the reduced filament polarization due to the depolarizing field (see Oldenbourg and Ruiz, 1989).

This estimate of filament birefringence assumes that the dielectric constant $\epsilon_m$ of the filament material is isotropic and does not possess any intrinsic birefringence. This is a valid assumption for microtubules, which were shown to have very little, if any, intrinsic birefringence (Sato et al., 1975). Therefore, microtubules exhibit almost exclusively form birefringence.

The birefringence $\Delta n$ of a coherence region containing one filament is then calculated using

$$\Delta n = n_\parallel - n_\perp = \sqrt{\epsilon_\parallel} - \sqrt{\epsilon_\perp} \tag{4}$$

and substituting $\epsilon_\parallel$ and $\epsilon_\perp$ with the right-hand sides of Eqs. 2 and 3, respectively. Because we are considering only small volume fractions $f$, we expand the new expression in a Taylor series around $f = 0$ and keep only the first order:

$$\Delta n = \frac{(\epsilon_m - \epsilon_s)^2}{2\sqrt{\epsilon_s}(\epsilon_s + \epsilon_m)} f = \Delta n' f, \quad \text{with} \tag{5}$$

$$\Delta n' = \frac{(\epsilon_m - \epsilon_s)^2}{2\sqrt{\epsilon_s}(\epsilon_s + \epsilon_m)} \tag{6}$$

$\Delta n'$ is called the specific birefringence or the birefringence per volume fraction. For volume fractions of ~1%, the second-order coefficient of the Taylor series gives only a 1% correction to the first order and can safely be neglected. As shown below, $\Delta n'$ was measured experimentally and is known from the literature.

Next we consider the retardance $R$ of the coherence region, which is the product of the birefringence and the path length. The path length extends parallel to the optic axis and equals the long axis of the coherence region; hence we multiply Eq. 5 by $2n\lambda/(\mathrm{NA}^2)$ and substitute $f$ with the right-hand side of Eq. 1 to calculate the retardance $R$:

$$R = \Delta n\ 2n\lambda/(\mathrm{NA}^2) = \Delta n' \frac{\bar{V}}{\lambda/(2\mathrm{NA})} = \Delta n' \bar{V} \frac{2\mathrm{NA}}{\lambda} \tag{7}$$

This result is consistent with our experimental finding that the retardance of the coherence region, which is equivalent to the measured peak retardance of the filament, decreases with decreasing numerical aperture of the imaging system.

Our last goal is to find an expression for the retardance area, which we found to be independent of NA in our experimental retardance images. To this end we multiply the retardance $R$ by the linear cross section of the coherence region, based on the approximation that $R$ is constant over the coherence region that contains the filament and is zero everywhere else. The linear extent of the cross section is ($\lambda/2\mathrm{NA}$), which will, in fact, render the retardance area independent of NA:

$$\bar{R} = R(\lambda/2\mathrm{NA}) = \Delta n' \bar{V} \tag{8}$$

In fact, $\bar{R}$ is only dependent on material parameters $\Delta n'$ and $\bar{V}$ and not on instrumental parameters of the optical set-up.

We now will show that our theoretical predictions are in agreement with our experimental results and with values for $\Delta n'$ and $\bar{V}$ known from the literature. Measurements of the specific birefringence $\Delta n'$ for oriented microtubule arrays were reported by two groups. Sato et al. (1975) measured the retardance of metaphase spindles isolated from oocytes of the sea star. Careful imbibition experiments allowed them to fit their data to the theory of Wiener, measuring a refractive index for the MT rodlets of 1.512 and a specific birefringence $\Delta n' = 0.025$. Hard and Allen (1985) published measurements of the specific birefringence of microtubule solutions oriented by flow through a capillary. Their value of $\Delta n' = 0.023$ must be considered a lower limit, because the degree of flow alignment was not determined and is probably less than perfectly parallel.

We estimate the volume $\bar{V}$ per unit length of a microtubule by using an average outer diameter of 24 nm (Amos, 1979), leading to $\bar{V} = 12^2 \cdot \pi = 450\ \mathrm{n}^2$. Hence $\Delta n' \cdot \bar{V} = 11.25\ \mathrm{nm}^2$, which is not far from the measured value of 7.5 nm$^2$ for the retardance area. We divide the retardance area by $\lambda/(2\mathrm{NA})$ to estimate the peak retardance of 0.058 nm, which is inside the error margin of the measured value of 0.07 ± 0.02 nm.

## DISCUSSION

Our theory of microtubule birefringence is surprisingly accurate in predicting the measured values, considering the simplicity of its assumptions and of the optical concepts invoked. A more complete description would certainly have to be based on scattering theory and wave optical concepts of image formation, to explain the detailed features of the filament image, such as the subsidiary maxima and their negative retardance. For example, scattering theory was recently applied to analyze the orientation-dependent visibility of thin rods under oblique illumination (Arimoto and Murray, 1996). However, the success of our conceptual theory in predicting experimental findings, without any adjustable parameter, is a strong argument for the role of the coherence region as we describe it and the effect of the filament on the dielectric anisotropy of this region. The theory also establishes the retardance area as the product of the specific birefringence of the filament material and the volume per unit length of the filament. Both quantities are material parameters that are independent of the optical set-up.

Our current theory of single particle birefringence assumes the particle to be in focus for the measurement. The theory does not incorporate the effect of defocusing on the predicted particle birefringence, nor does it apply to measurements of extended birefringent objects using imaging optics of finite numerical aperture (NA). Sato et al. (1975) found at low to moderate NA, that the measured birefringence of the extended spindle birefringence was independent of NA. A more complete theory will incorporate these situations to give predictions about the point and line spread functions of subwavelength birefringent particles and the imaging of extended objects.

Our measurements of crossed axonemes give first experimental results for objects that are extended in the $z$ direction. Inside the overlap region of crossed and closely spaced axonemes, we have measured the expected decrease in peak retardance and a 90° turn of the slow axis direction, depending on which of the two axonemes is closer to focus. This flip in slow axis orientation occurred within a distance of 0.4 $\mu$m of stage travel along the $z$ axis. On one hand, compared to the axoneme diameter of $\sim$0.2 $\mu$m, this distance seemed long, and we attributed the apparent increase, at least in part, to the mismatch in refractive index at the glass-water interface. On the other hand, the distance of 0.4 $\mu$m is about one-quarter of the axial extend of the point spread function of the 1.4 NA objective lens. At first sight, it seems surprising that within this short optical distance a 90° turn of the measured azimuth can be observed. We believe that this result indicates that the axial resolution in polarized light microscopy and probably in other phase-dependent, partially coherent imaging modes is considerably higher than predicted by the point spread function (see also Inoué, 1989). The result, however, is not yet understood on the basis of a rigorous theory, but seems to indicate that resolution enhancement is possible if magnitude and azimuth are measured together in polarized light microscopy. Therefore, it seems particularly promising to develop 3-D deconvolution methods for polarized light microscopy, to take full advantage of the high spatial resolution obtainable with this technique.

It is a great pleasure to contribute this article to the special issue in honor of Donald L. D. Caspar's 70th birthday. One of the authors, Rudolf Oldenbourg, was a postdoc in Don Caspar's laboratory at the Rosenstiel Center for Basic Medical Sciences at Brandeis University. There Dr. Oldenbourg worked with virus liquid crystals, among them, of course, tobacco mosaic virus. It was an observation of another virus, however, that got Dr. Caspar excited at the time. He had just spent a sabbatical at Nagoya University in Japan, where he was able to watch single, fluorescently labeled, 2-$\mu$m-long Pf1 bacteriophages wiggling from thermal motion directly under the light microscope. His characteristic enthusiasm for this observation started to make Dr. Oldenbourg aware of the revolution unfolding around the light microscope. This traditional tool is now able to visualize single, fluorescently labeled macromolecular assemblies such as the 6-nm-thick Pf1 or, as demonstrated in this article, unlabeled 24-nm-thick microtubules. The advances in light microscopy that made this possible were largely due to Shinya Inoué, whom all three authors wish to thank for his continued inspiration, stimulating discussions, and insightful comments and ideas contributed to this work.

Financial support was provided in part by the National Institute of General Medical Sciences, National Institutes of Health, grants GM49210 awarded to RO, GM24364 awarded to EDS, and a MBL Fries Fellowship awarded to PTT.

## REFERENCES

Allen, R. D., and N. S. Allen. 1983. Video-enhanced microscopy with a computer frame memory. *J. Microsc.* 129:3–17.

Allen, R. D., J. L. Travis, N. S. Allen, and H. Yilmaz. 1981. Video-enhanced contrast polarization (AVEC-POL) microscopy: a new method applied to the detection of birefringence in the motile reticulopodial network allogromia laticollaris. *Cell Motil.* 1:275–289.

Amos, L. A. 1979. Structure of microtubules. *In* Microtubules. K. Roberts and J. S. Hyams, editors. Academic Press, London. 1–64.

Arimoto, R., and J. M. Murray. 1996. Orientation-dependent visibility of long thin objects in polarization-based microscopy. *Biophys. J.* 70: 2969–2980.

Bell, C. W., C. Fraser, W. S. Sale, W.-J. Y. Tang, and I. R. Gibbons. 1982. Preparation and purification of dynein. *In* The Cytoskeleton. L. Wilson, editor. Academic Press, New York. 373–397.

Born, M., and E. Wolf. 1980. Principles of Optics, 6th Ed. Pergamon Press, Elmsford, NY.

Bragg, W. L., and A. B. Pippard. 1953. The form birefringence of macromolecules. *Acta Crystallogr.* 6:865–867.

Chamot, E. M., and C. W. Mason. 1958. Handbook of Chemical Microscopy, 2nd Ed. John Wiley and Sons, New York.

Dustin, P. 1984. Microtubules, 2nd Ed. Springer Verlag, New York.

Endow, S. A., S. J. Kang, L. L. Satterwhite, M. D. Rose, V. P. Skeen, and E. D. Salmon. 1994. Yeast Kar3 is a minus-end microtubule motor protein that destabilized microtubules preferentially at the minus ends. *EMBO J.* 13:2708–2713.

Hard, R., and R. D. Allen. 1985. Flow birefringence of microtubules and its relation to birefringence measurements in cells. *Cell Motil.* 5:31–51.

Hartshorne, N. H., and A. Stuart. 1960. Crystals and the Polarising Microscope: A Handbook for Chemists and Others, 3rd Ed. Arnold, London.

Hecht, E. 1987. Optics. Addison-Wesley Publishing Co., Reading, PA.

Inoué, S. 1953. Polarization optical studies of the mitotic spindle. I. The demonstration of spindle fibers in living cells. *Chromosoma.* 5:487–500.

Inoué, S. 1981. Video image processing greatly enhances contrast, quality and speed in polarization-based microscopy. *J. Cell Biol.* 89:346–356.

Inoué, S. 1986. Video Microscopy. Plenum Press, New York.

Inoué, S. 1989. Imaging of unresolved objects, superresolution and precision of distance measurement with video microscopy. *In* Methods in Cell Biology. D. L. Taylor and Y.-L. Wang, editors. Academic Press, New York. 85–112.

Inoué, S., and W. L. Hyde. 1957. Studies on depolarization of light at microscope lens surfaces. II. The simultaneous realization of high resolution and high sensitivity with the polarizing microscope. *J. Biophys. Biochem. Cytol.* 3:831–838.

Inoué, S., J. Mole-Bajer, and A. S. Bajer. 1985. Three-dimensional distribution of microtubules in *Haemanthus* endosperm cells. *In* Microtubules and Microtubule Inhibitors. M. deBrabander and J. deMey, editors. Elsevier Science Publishing Company, Amsterdam. 269–276.

Inoué, S., and R. Oldenbourg. 1995. Microscopes. *In* Handbook of Optics, 2nd Ed. M. Bass, editor. McGraw-Hill, New York. 17.1–17.52.

Inoué, S., and K. R. Spring. 1997. Video Microscopy, 2nd Ed. Plenum Press, New York.

Kubota, H., and S. Inoué. 1959. Diffraction images in the polarizing microscope. *J. Opt. Soc. Am.* 49:191–198.

Linck, R. W., L. A. Amos, and W. B. Amos. 1985. Localization of tektin filaments in microtubules of sea urchin sperm flagella by immunoelectron microscopy. *J. Cell Biol.* 100:126–135.

McCrone, W. C. 1991. Light microscopy. *In* Physical Methods of Chemistry. B. W. Rossiter and J. F. Hamilton, editors. John Wiley and Sons, New York. 343–443.

Oldenbourg, R. 1991. Analysis of edge birefringence. *Biophys. J.* 60: 629–641.

Oldenbourg, R. 1996. A new view on polarization microscopy. *Nature.* 381:811–812.

Oldenbourg, R., S. Inoué, R. Tiberio, A. Stemmer, G. Mei, and M. Skvarla. 1996. Standard test targets for high resolution light microscopy. *In* Nanofabrication and Biosystems: Integrating Material Science, Engineering and Biology. H. C. Hoch, L. W. Jelinsky, and H. Craighead, editors. Cambridge University Press, Cambridge. 123–138.

Oldenbourg, R., and G. Mei. 1995. New polarized light microscope with precision universal compensator. *J. Microsc.* 180:140–147.

Oldenbourg, R., and T. Ruiz. 1989. Birefringence of macromolecules: Wiener's theory revisited, with applications to DNA and tobacco mosaic virus. *Biophys. J.* 56:195–205.

Sato, H., G. W. Ellis, and S. Inoué. 1975. Microtubular origin of mitotic spindle form birefringence: demonstration of the applicability of Wiener's equation. *J. Cell Biol.* 67:501–517.

Schmidt, W. J. 1924. Die Bausteine des Tierkörpers in polarisiertem Lichte. Cohen, Bonn.

Schmidt, W. J. 1937. Die Doppelbrechung von Karyoplasma, Zytoplasma und Metaplasma. Bornträger, Berlin.

Shurcliff, W. A. 1962. Polarized Light, Production and Use. Harvard University Press, Cambridge, MA.

Tilney, L. G., J. Bryan, D. J. Bush, K. Fujiwara, M. S. Mooseker, D. B. Murphy, and D. H. Snyder. 1973. Microtubules: evidence for 13 protofilaments. *J. Cell Biol.* 59:267–275.

Tran, P., E. D. Salmon, and R. Oldenbourg. 1995. Quantifying single and bundled microtubules with the polarized light microscope. *Biol. Bull.* 189:206.

Visser, T. D., J. L. Oud, and G. J. Brakenhoff. 1992. Refractive index and axial distance measurements in 3-D microscopy. *Optik.* 90:17–19.

Voter, W. A., and H. P. Erickson. 1984. The kinetics of microtubule assembly. Evidence for a two-stage nucleation mechanism. *J. Biol. Chem.* 259:10430–10438.

Walker, R. A., E. T. O'Brien, N. K. Pryer, M. F. Soboeiro, W. A. Voter, H. P. Erickson, and E. D. Salmon. 1988. Dynamic instability of individual microtubules analyzed by video light microscopy: rate constants and transition frequencies. *J. Cell Biol.* 107:1437–1448.

Wiener, O. 1912. Die Theorie des Mischkörpers für das Feld der stationären Strömung. *Abh. Math.-Phys. Klasse königlich sächsischen Ges. Wiss.* 32:509–604.

Wilson, T., and C. Sheppard. 1984. Theory and Practice of Scanning Optical Microscopy. Academic Press, London.